SAE INTERNATIONAL

Physics-Based Modeling and Transient Validation of an Organic Rankine Cycle Waste Heat Recovery System for a Heavy-Duty Diesel Engine

Bin Xu
Clemson-ICAR

Xiaobing Liu
BorgWarner Inc

John Shutty
BorgWarner Automotive

Paul Anschel
BorgWarner Turbo Systems

Simona Onori, Zoran Filipi, and Mark Hoffman
Clemson-ICAR

Abstract

This paper presents an Organic Rankine Cycle (ORC) system model for heavy-duty diesel (HDD) applications. The dynamic, physics-based model includes: heat exchangers for parallel exhaust and EGR circuits, compressible vapor working fluid, distribution and flow control valves, a high pressure pump, and a reservoir. A finite volume method is used to model the evaporator, and a pressure drop model is included to improve the accuracy of predictions. Experimental results obtained on a prototype ORC system are used for model calibration and validation. Comparison of predicted and measured values under steady-state conditions is pursued first, followed by the analysis of selected transient events. Validation reveals the model's ability to track real-world temperature and pressure dynamics of the ORC system. Therefore, this modeling framework is suitable for future system design studies, optimization of ORC power generation, and as a basis for development of control-oriented ORC models.

Introduction

U.S. CO_2 emission regulations call for a 20% reduction by 2020 relative to 2010 [1]. Heavy duty vehicles account for 7% of all onroad vehicles and about 30% of the U.S. transportation energy usage [2]; therefore, the impact of their fuel consumption on fleet business and the economy is significant. Even with recent technological advances in long haul truck aerodynamic packages and light-weighting, engine efficiency remains a key factor in CO_2 emission reduction strategies.

As most in-cylinder approaches have gradually been exhausted over the past decade, ORC has been gaining traction as a method for system level efficiency improvement [3,4,5,].

Several experimental studies explored ORC utilization for waste heat recovery (WHR) and reported encouraging results. Endo et al. [4] implemented a Rankine cycle device with a passenger car engine and reported 13.2% thermal efficiency improvement at 100 km/h constant vehicle speed. Their innovative evaporator was integrated with the cylinder head to reduce heat loss and improve packaging. A study by Teng et al. [6] achieved 3~5% HDD fuel savings by utilizing ORCWHR technology with ethanol as a working fluid. In their system, EGR and exhaust gas boilers are connected in series and power generated by the turbine expander is absorbed by an air brake compressor. Seher et al. [7] utilized a Rankine cycle system coupled to a 12L HDD engine to generate up to 9kW at the B75 operating point. In their experiments, water was selected as working fluid and power was extracted from a turbine expander.

Realization of the full efficiency improvement potential of ORCWHR depends on rigorous simulation studies of system design and optimized control. The existing body of work on ORC-WHR system modeling can be categorized based on heat exchanger modeling approach into: (i) the finite volume method, and (ii) the moving boundary method.

The finite volume method typically yields higher accuracy, but slower computation speed. Quoilin [8] developed a dynamic ORCWHR system model based on the finite volume method. However, the model was validated with limited experimental data, which lacked transient engine and ORC operating conditions. Feru also developed an ORC-WHR model for HDD using the finite volume method and utilized a large amount of experimental data for model identification and validation [9]. However, pressure drop across the evaporator was neglected, which, depending on heat exchanger design, can lead to significant inaccuracy. Compact heat exchangers with small hydraulic diameters have become a prominent design, achieving higher heat transfer with the side effect of increased pressure drop [10]. Several investigations have been conducted to characterize nanofluid heat transfer [11].

Many authors choose to minimize vapor superheating and maximize working fluid mass flow to enhance ORC power generation [12,13,14]. In that case, accurate determination of saturation temperature, which depends on evaporator pressure, is essential. Inclusion of evaporator pressure drop is important for accurate prediction of the working fluid vapor quality, thus maximizing power generation while ensuring the safety of the turbine expander. These considerations create impetus for the work presented here.

Moving boundary heat exchanger models are often utilized for control purposes [15,16,17,18]. The main advantage of moving boundary heat exchanger modeling is reduced computation cost. This is a critical feature for real-time applications in model-based control. Yet, the moving boundary heat exchanger model has inferior accuracy relative to the finite volume model, and latter has been preferred in offline system optimization studies. This motivates efforts to expand the applicability of reduced finite volume heat exchanger models and enable online ORC-WHR optimization. A recent study by Feru [14] demonstrates the value of a high-fidelity evaporator model as a basis for creating a virtual ORC plant.

Overall, ORC-WHR has attracted significant attention, but publications in this area are mainly focused on control, while publications focused on high-fidelity, dynamic, physics-based models are relatively scarce. Therefore, our main objective is to develop and validate a physics-based ORC-WHR model that includes predictions of evaporator pressure drop, and demonstrate its ability to capture both steady-state and transient behavior.

This paper introduces the configuration of the ORC-WHR system first, followed by detailed descriptions of component models. Particular attention is devoted to the application of finite volume method and inclusion of evaporator pressure drop to achieve high-fidelity of predictions. Model calibration results are presented next, followed by transient model validation results. The paper ends with discussion and conclusions.

Experimental ORC-WHR System Configuration

The system components are connected to create an ORC loop, specifically: (i) a low pressure working fluid supply pump , (ii) a high pressure pump, (iii) two valves which distribute the working fluid between the evaporators, (iv) two parallel evaporators, (v) an exhaust bypass valve, (vi) a valve upstream of the turbine expander, (vii) a valve before the turbine to bypass liquid working fluid when the system is in warm-up or cool-down state, (viii) turbine expander for generation of electricity, (ix) condenser downstream of the turbine, and (x) expansion tank between condenser and low pressure pump to buffer the working fluid flow. Ethanol is selected as working fluid because of its favorable physical characteristics and environmental friendliness.

Modern diesel engines typically operate with high pressure exhaust gas recirculation (EGR), making the EGR stream an attractive heat source for a diesel WHR system. The inclusion of EGR as a heat source (along with the tailpipe exhaust flow) creates options for the connection of the two heat exchangers: in series or in parallel. The parallel connection is suitable for high mass flow with low pressure loss because the cross sectional area of working fluid's flow path is increased. A series evaporator connection produces higher working fluid vapor temperatures because the long flow path aides superheating. Considering that higher mass flow has been proven beneficial for power generation [9], the parallel configuration is chosen and shown in Figure 1.

The ORC-WHR system is coupled to a 13L heavy duty diesel engine. The only connections between engine and ORC-WHR system are the tail pipe (TP) and EGR evaporators, shown in Figure 1. During normal operating conditions, exhaust gas flows through the TP evaporator to evaporate the working fluid. A TP evaporator bypass valve is installed to protect the ORC-WHR working fluid from overheating and subsequent degradation when the engine operates at high load. The EGR evaporator replaces the stock EGR intercooler. Due to EGR evaporator outlet temperature constraints, there is no bypass valve installed in the EGR line. The working fluid mass flow to the parallel branches is controlled by valves located between the pump and their respective evaporator.

ORC Component Model Descriptions

The modeling of each component within the ORC system is presented as follows:

Evaporators and Condenser

The ORC evaporator is the key component, facilitating energy transport from exhaust gas to the working fluid. Mass balance, energy balance and momentum balance are applied within the evaporator model. Several assumptions are made for the heat exchanger model, such as: (i) axial heat conduction in working fluid, wall and exhaust gas are neglected, (ii) the time varying momentum balance term is neglected because of its fast dynamics, (iii) vapor inside heat exchanger is incompressible, and (iv) the wall temperature in the radial direction is uniform. The fundamental equations governing the evaporators are presented for the TP evaporator only. However, the same equations hold true for the EGR evaporator.

Mass balance

$$\frac{\partial A\rho}{\partial t} + \frac{\partial \dot{m}}{\partial z} = 0$$

(1.1)

where A is the section area of flow, ρ is fluid density, $\dot{m}$ is fluid mass flow rate, and z is spatial position in axial direction.

Working fluid and TP/EGR energy balance

$$\frac{\partial\left(A_2\rho h - A_1 p\right)}{\partial t} + \frac{\partial \dot{m}h}{\partial z} = \pi DU\Delta T$$

(1.2)

where A_1 is section area of working fluid flow in heat exchanger, p is the fluid pressure in the heat exchanger, A_2 is heat transfer area between the working fluid and the wall, U is the heat transfer coefficient, and ΔT is the temperature difference between the working fluid and the wall.

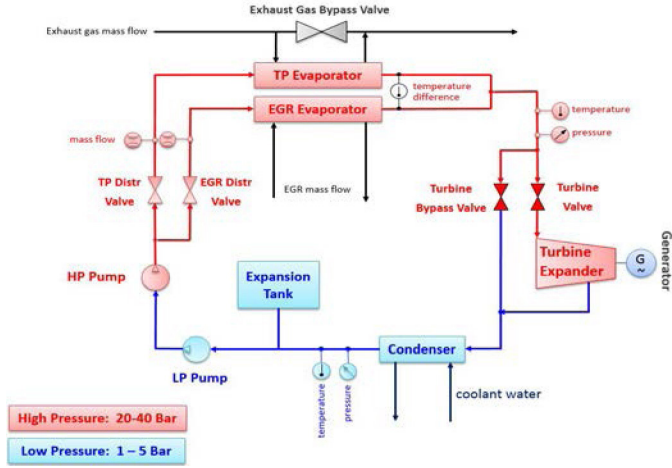Figure 1. Schematic of ORC-WHR system

Wall energy balance

$$A_{w,cross}c_p\rho L\frac{dT_w}{dt} = A_1 U_1\Delta T_1 + A_2 U_2\Delta T_2$$

(1.3)

The wall is the heat transfer media, absorbing heat from the source and releasing heat to the working fluid. Subscript 1 and 2 represent the heat source side and heat recipient side of the wall respectively. L is the wall length in the axial direction, c_p is wall heat capacity, and $A_{w,cross,}$ is wall section area.

In order to solve eqs. (1.1) and (1.2), the PDE is reduced to an ODE as follows,

$$\frac{dm}{dt} = \dot{m}_{in} - \dot{m}_{out}$$

(1.4)

$$\frac{d\left(mh - vp\right)}{dt} = \dot{m}_{in}h_{in} - \dot{m}_{out}h_{out} + \pi DU\Delta T$$

(1.5)

Then, the ODE eqs. (1.3) - (1.5) can be solved with explicit method as follows:

$$T_{w,t(k+1)} = T_{w,t(k)} + \frac{\left(A_1 U_1\Delta T_1 + A_2 U_2\Delta T\right)}{A_{w,cross}c_p\rho L}\Delta t$$

(1.6)

$$m_{t(k+1)} = m_{t(k)} + \left(\dot{m}_{in} - \dot{m}_{out}\right)\Delta t$$

(1.7)

$$\left(mh\right)_{t(k+1)} = \left(mh\right)_{t(k)} + \frac{d\left(vp\right)}{dt} + \left(\dot{m}_{in}h_{in} - \dot{m}_{out}h_{out} + \pi DU\Delta T\right)\Delta t$$

(1.8)

where k is kth time step, Δt is length of time step, $d(vp)/dt$ is solved by eqs. (6.1), (6.2), (6.3), and v is the volume of one discretized cell. The exhaust gas mass flow rate is assumed to be uniform along the whole evaporator because of its fast dynamics. Working fluid and exhaust gas energy balance share the same eq. (1.8). Altogether, there are four equations to be solved for each cell: wall energy balance eq. (1.6); working fluid mass balance eq. (1.7); working fluid energy balance eq. (1.8); and exhaust gas energy balance eq. (1.8). Each evaporator is divided into 30 discrete cells. The results are obtained by applying eqs. (1.6), (1.7), (1.8) in each cell.

Momentum balance

$$\frac{dI}{dt} = F_p + F_{fr} + F_g + F_a$$

(1.9)

where I is the momentum of fluid, F_p is pressure, F_{fr} is wall friction force, F_g is gravitational force, and F_a is acceleration force. All four forces are in heat exchanger axial direction. Neglecting dynamics to momentum, eq. (1.9) can be simplified to:

$$0 = F_p + F_{fr} + F_g + F_a$$

(1.10)

Applying mass balance on TP evaporator working fluid we arrive at:

$$\frac{\partial m_{f,TP,i}}{\partial t} = \dot{m}_{f,TP,in,i} - \dot{m}_{f,TP,out,i}$$

(1.11)

where f is working fluid, TP is tail pipe evaporator, in and out denote spatial context, and i is discretized cell number. Applying energy balance to the working fluid in TP evaporator:

$$\frac{\partial\left(m_{f,TP,i}h_{f,TP,i}\right)}{dt} = \frac{\partial\left(A_{f,TP,cross}p_{f,TP,i}\right)}{dt}$$
$$+ \left(\dot{m}_{f,TP,in,i}h_{f,TP,in,i} - \dot{m}_{f,TP,out,i}h_{f,TP,out,i}\right)$$
$$+ A_{f,w,TP,i}U_{f,w,TP,i}\left(T_{w,TP,i} - T_{f,TP,i}\right)$$

(1.12)

Given the assumption that wall temperature in the radial direction is uniform, the wall temperature possesses only an axial gradient. Therefore, application of energy balance on the wall between working fluid and exhaust gas in TP evaporator takes on the form:

$$A_{w,TP,cross}c_{p,w}\rho_w\Delta z\frac{dT_{w,TP,i}}{dt}$$
$$= A_{e,w,TP,i}U_{e,w,TP,i}\left(T_{e,TP,i} - T_{w,TP,i}\right)$$
$$- A_{f,w,TP,i}U_{f,w,TP,i}\left(T_{w,TP,i} - T_{f,TP,i}\right)$$

(1.13)

where w is wall and e is exhaust gas. Additionally, apply energy balance on exhaust gas in TP evaporator yields:

$$\frac{\partial\left(m_{e,TP,i}h_{e,TP,i}\right)}{dt} = \frac{\partial\left(A_{e,TP,cross}p_{e,TP,i}\right)}{dt} + \left(\dot{m}_{e,TP,in,i}h_{e,TP,in,i}\right.$$
$$- \dot{m}_{e,TP,out,i}h_{e,TP,out,i}\right)$$
$$+ A_{e,w,TP,i}U_{e,w,TP,i}\left(T_{w,TP,i} - T_{e,TP,i}\right)$$

(1.14)

Pressure Drop

Evaporator pressure drop can be significant if a small hydraulic diameter is utilized. The hydraulic diameter of the experimental working fluid tube is 4 mm with a total length over 50 meters, creating a pressure drop substantially higher than the 1mbar described in [19]. A high pressure drop results in evaporation temperature alterations across the evaporator, which affects model accuracy.

The working fluid pressure drop in each discretized cell can be calculated through application of momentum balance on the TP evaporator working fluid [20]. Considering computation time, only three pressure drops are calculated based on working fluid phase (liquid, two-phase, and vapor). Details of the pressure drop derivation are included in the Appendix. For brevity, only the final form of the expression is denoted in eq. (2.1), (2.2), (2.3).

Liquid phase region:

$$\Delta p_l = \int_{Z_1}^{Z_{a_{sat}}} \left(\frac{dp}{dz}\right)dz = \int_{Z_1}^{Z_{a_{sat}}} -\left(\frac{2f_lG^2}{\rho_ld_h} + \frac{1}{A}\frac{d}{dz}\left(\frac{G^2A}{\rho_l}\right)\right)dz =$$
$$-\left(\sum_{i=1}^{a_{sat}}\left(\frac{2\bar{f}_{li}\bar{G}_i^2}{\bar{\rho}_{li}d_h}\Delta z\right) + \left[\frac{G_{a_{sat}+1}^2}{\rho_{la_{sat}+1}}\right] - \left[\frac{G_1^2}{\rho_{l1}}\right]\right)$$

(2.1)

where *f* is fraction, *G* is mass flux, and d_h is hydraulic diameter, *a* is the ath boundary of the discretized evaporator and ranges from 1 to $N+1$, *N* is the total number of discretized cells, and subscript '*sat*' refers to saturated liquid. Pressure drop is calculated at the boundary of each cell. Therefore *a* has $N+1$ values.

Vapor phase region:

$$\Delta p_v = \int_{Z_{a_{vap}}}^{Z_{N+1}} \left(\frac{dp}{dz}\right)dz = \int_{Z_{a_{vap}}}^{Z_{N+1}} -\left(\frac{2f_vG^2}{\rho_vd_h} + \frac{1}{A}\frac{d}{dz}\left(\frac{G^2A}{\rho_v}\right)\right)dz =$$
$$-\left(\sum_{i=a_{vap}}^{N+1}\left(\frac{2\bar{f}_{v,i}\bar{G}_i^2}{\bar{\rho}_{v,i}d_h}\Delta z\right) + \left[\frac{G_{N+1}^2}{\rho_{v,N+1}}\right] - \left[\frac{G_{a_{vap}}^2}{\rho_{v,a_{vap}}}\right]\right)$$

(2.2)

where subscript '*vap*' refers to saturated vapor.

Two-phase region:

$$\Delta p_{tp} = \int_{Z_{a_{sat}+1}}^{Z_{a_{vap}-1}} \left(\frac{dp}{dz}\right)dz = -\left(\sum_{i=a_v}^{N}\left(\bar{\Phi}_v^2\frac{2\bar{f}_v\bar{G}_i^2\bar{x}^2}{\bar{\rho}_vd_h}\Delta z\right) + \right.$$
$$\left[\frac{G_{a_{vap}}^2x_{a_{vap}}^2}{\rho_{v(a_{vap})}\alpha_{a_{vap}}}\right] - \left[\frac{G_{a_{sat}+1}^2x_{a_{sat}+1}^2}{\rho_{v(a_{sat}+1)}\alpha_{a_{sat}+1}}\right] + \left[\frac{G_{a_{vap}}^2\left(1-x_{a_{vap}}\right)^2}{\rho_{l(a_{vap})}\left(1-\alpha_{a_{vap}}\right)}\right] -$$
$$\left.\left[\frac{G_{a_{sat}+1}^2\left(1-x_{a_{sat}+1}\right)^2}{\rho_{l(a_{sat}+1)}\left(1-\alpha_{a_{sat}+1}\right)}\right]\right)$$

(2.3)

where void fraction α and vapor quality *x* are denoted in eq. (3.11) and (3.12).

Finally, total pressure drop across the evaporator is obtained:

$$\Delta p_{evap} = \Delta p_l + \Delta p_v + \Delta p_{tp}$$

(2.4)

Experimental validation will utilize total evaporator pressure drop for validation because the pressure drops of the respective phases are difficult to measure.

Evaporator Heat Transfer

The calculation of heat transfer in the heat exchangers is divided into two sections: exhaust gas and working fluid. In the exhaust gas section, all the discretized cells share the same time dependent heat transfer coefficient. In the working fluid section, the calculation of heat transfer is separated by working fluid phase with zones corresponding to liquid, two-phase and gaseous working fluid. Each phase has a distinct heat transfer coefficient calculation based on the working fluid quality, mass flow rate, and pressure. Therefore, the heat transfer coefficient in working fluid side is both time and spatially dependent.

Exhaust Gas and EGR Heat Transfer

For the calculation of heat transfer coefficient between exhaust gas and wall Reynold's number is utilized [21].

$$\text{Re}_{e,TP} = \frac{\dot{m}_{e,TP}d_{e,TP}}{A_{e,TP,cross}v_d}$$

(3.1)

where *Re* is Reynolds number, *d* is hydraulic diameter, and v_d is dynamic viscosity. Gnielinski gave eq. (3.2) as a friction factor for concentric tubes [22], which is selected because of the concentric tube structure of the evaporator:

$$\xi_{e,TP} = \left(1.8\log_{10}\text{Re}_{e,TP}^* - 1.5\right)^{-2}$$

(3.2)

$$\text{Re}_{e,TP}^* = \text{Re}_{e,TP}\frac{\left(1+a^2\right)\ln a + \left(1-a\right)}{\left(1-a^2\right)\ln a}$$

(3.3)

where ξ is friction factor, $a = \frac{d_{in}}{d_{out}}$, d_{in} and d_{out} are inner and outer diameters of concentric tube respectively. Prandtl number is also utilized, eq. (3.4), to arrive at a calculation for thermal conductivity of the exhaust gas, eq. (3.5).

$$\text{Pr}_{e,TP} = \frac{v_{d,e,TP}c_{p,e,TP}}{k_{e,TP}}$$

(3.4)

$$k_{1,e,TP} = 1.07 + \frac{900}{\text{Re}_{e,TP}} - \frac{0.63}{\left(1+10\text{Pr}_{e,TP}\right)}$$

(3.5)

A Nusselt number expression, eq. (3.6), for a concentric tube with insulated outer pipe wall is selected based on the structure of heat exchanger [23]:

$$Nu_{e,TP} = \frac{\left(\xi_{e,TP}/8\right)\mathrm{Re}_{e,TP}\,\mathrm{Pr}_{e,TP}}{k_{1,e,TP}+12.7\sqrt{\xi_{e,TP}/8}\left(\mathrm{Pr}_{e,TP}^{2/3}-1\right)}\left[1+\left(\frac{d_{e,TP}}{l}\right)^{2/3}\right]$$

(3.6)

where l is length of the pipe in the heat exchanger.

After the Nusselt number is obtained, the heat transfer coefficient between exhaust gas and wall can be calculated with eq. (3.7) from [24]. The experimental evaporator construction differs slightly from concentric tubes, so a heat transfer coefficient multiplier is introduced in the implementation stage.

$$U_{e,w,TP} = \frac{Nu_{e,TP}k_{e,TP}}{d_{e,TP}}$$

(3.7)

Working Fluid Heat Transfer

For the calculation of pure liquid and pure vapor heat transfer coefficients between working fluid and wall, eq. (3.8) and (3.9) are utilized [23]. These heat transfer coefficients are selected because of the helical coil heat exchanger structure.

$$\xi_{f,TP,i} = 0.0075\left(\frac{d_{f,TP}}{D_{f,TP}}\right)^{0.5}+\frac{0.079}{\mathrm{Re}_{f,TP,i}^{0.25}}$$

(3.8)

$$U_{f,w,TP,i} = \frac{\left(\xi_{f,TP,i}/8\right)\mathrm{Re}_{f,TP,i}\,\mathrm{Pr}_{f,TP,i}}{1+12.7\sqrt{\xi_{e,TP,i}/8}\left(\mathrm{Pr}_{e,TP,i}^{2/3}-1\right)}\cdot\frac{k_{f,TP,i}}{d_{f,TP}}$$

(3.9)

For calculation of the two-phase heat transfer coefficient between the working fluid and the wall, a vertical tube two-phase heat transfer coefficient is used [23], which shares a similar structure to the helical coil. $U_{f,w,TP,bubble}$ and $U_{f,w,TP,dew}$ are calculated using the single phase eq. (3.9).

$$U_{f,TP,tp} = \left\{(1-x)^{0.01}\left[(1-x)+1.9x^{0.4}\left(\frac{\rho_{f,bubble}}{\rho_{f,dew}}\right)^{0.35}\right]^{-2.2}\right.$$
$$+x^{0.01}\left[\frac{U_{f,TP,dew}}{U_{f,TP,bubble}}\left(1\right.\right.$$
$$\left.\left.\left.+8(1-x)^{0.7}\left(\frac{\rho_{f,bubble}}{\rho_{f,dew}}\right)^{0.67}\right)\right]^{-2}\right\}^{-0.5}$$

(3.10)

Void fraction, α, and vapor quality, x, are calculated from eqs. (3.11) and (3.12), respectively [25].The expressions of Zivi [25] were chosen because of their robustness over a large range of pressure and mass flow rates.

$$\alpha_{f,TP,i} = (1+\frac{1-x_{f,TP,i}}{x_{f,TP,i}}\left(\frac{\rho_{f,dew}}{\rho_{f,bubble}}\right)^{0.67})^{-1}$$

(3.11)

$$x_{f,TP,i} = \frac{h_{f,TP,i}-h_{f,TP,bubble}}{h_{f,TP,dew}-h_{f,TP,bubble}}$$

(3.12)

The EGR evaporator utilizes the same equations, but different geometric dimensions, evaporator efficiency and the exhaust gas side heat transfer coefficient multiplier. The condenser utilizes lumped parameters rather than finite volume method to reduce computational cost.

Pump

The fundamental function of the pump is to maintain working fluid mass flow rate and system pressure. A positive displacement pump is utilized due to the high downstream pressure requirement. Generally, the mass flow rate of a positive displacement pump is nearly linear with respect to pump speed. Therefore, a linear relationship is assumed between the pump speed N_{pump} and mass flow rate $\dot{m}_{pump}$ as follows:

$$\dot{m}_{pump} = f(N_{pump}) = a_{pump}N_{pump}+b_{pump}$$

(4.1)

To predict the pump power consumption P_{pump}, a physics relation is built into the model via eq. (4.2) [9]:

$$P_{pump} = \frac{(\dot{m}_{pump}/\rho)(p_{out,pump}-p_{in,pump})}{\eta_{is,pump}}$$

(4.2)

where ρ is the pump upstream density, $p_{in,pump}/p_{out,pump}$ is upstream and downstream pressure and $\eta_{is,pump}$ is isentropic efficiency. The pump outlet temperature $T_{out,pump}$ is calculated as follows [9]:

$$T_{out,pump} = T_{in,pump}+\frac{(1-\eta_{is,pump})P_{pump}}{\dot{m}_{pump}c_{p,pump}}$$

(4.3)

where $c_{p,pump}$ is the upstream specific heat capacity of the working fluid.

Valves

The ORC-WHR system includes several valves: two mass flow distribution valves, one turbine upstream valve, and one turbine bypass valve. The two mass flow distribution valves are only exposed to liquid flow and are considered incompressible. All other valves encounter gaseous flow at some point during operation, so the working fluid must be considered compressible.

Incompressible Flow through Distribution Valves

Based on liquid incompressibility and conservation of mass, the pump mass flow rate has the following relation with flow through the parallel distribution valves.

$$\dot{m}_{pump} = \dot{m}_{TPEvapVlv}+\dot{m}_{EGREvapVlv}$$

(5.1)

A correlation is created to estimate mass flow rate between two mass flow distribution valves, which is expressed as function of valve opening as follows:

$$r_{\dot{m}} = c_{EvapVlv}\left(\frac{O_{TPEvapVlv}}{O_{EGREvapVlv}}\right)^{a_{EvapVlv}}$$

(5.2)

Finally, the two valve mass flow rates can be calculated.

$$\dot{m}_{TPEvapVlv} = \frac{r_m}{r_m + 1}\dot{m}_{pump}$$

(5.3)

$$\dot{m}_{EGREvapVlv} = \frac{1}{r_m + 1}\dot{m}_{pump}$$

(5.4)

In eq. (5.2), the two parameters $a_{EvapVlv}$ and $c_{EvapVlv}$ are obtained by fitting equations (5.3) and (5.4) with experimental data, which is done using the Matlab Genetic Algorithm (GA) function.

Compressible Flow through the Valves

Two valves control the compressible flow through the turbine expander, and the bypass around it. These valves ensure that the turbine expander is only exposed only to vapor. Flow of compressible fluid depends on whether the upstream and downstream pressure ratio is critical [26], i.e.:

If $\left(\frac{2}{\gamma+1}\right)^{\frac{\gamma}{\gamma-1}} \leq \frac{p_{out}}{p_{in}} \leq 1$, the flow state is subsonic and mass flow rate can be expressed as:

$$\dot{m} = OC_dA_0\sqrt{\frac{2\gamma}{\gamma-1}p_{in}\rho_{in}\left[\left(\frac{p_{out}}{p_{in}}\right)^{\frac{2}{\gamma}} - \left(\frac{p_{out}}{p_{in}}\right)^{\frac{\gamma+1}{\gamma}}\right]}$$

(5.5)

where $\gamma = c_p/c_v$ is heat capacity ratio of the working fluid vapor.
However, if $0 \leq \frac{p_{out}}{p_{in}} \leq \left(\frac{2}{\gamma+1}\right)^{\frac{\gamma}{\gamma-1}}$, then the flow state is supersonic and working fluid mass flow rate can be expressed as:

$$\dot{m} = OC_dA_0\left(\frac{2}{\gamma+1}\right)^{\frac{\gamma+1}{2(\gamma-1)}}\sqrt{\gamma p_{in}\rho_{in}}$$

(5.6)

Turbine upstream pressure is in the 5-60bar range and turbine downstream pressure is $\sim$1bar, therefore, the pressure ratio p_{out}/p_{in} varies only from 0.017~0.20, whereas the value of $\left(\frac{2}{\gamma+1}\right)^{\frac{\gamma}{\gamma-1}}$ is 0.5~0.6 in normal operating conditions. Thus, eq. (5.6) dominates.

Compressible Working Fluid Vapor

Transportation delay and pressure loss in the connecting pipes are neglected in the ORC system. Transportation delay can be divided into two cases: (i) liquid, and (ii) vapor. Liquid in the system is assumed to be incompressible, which means for any given pipe length, the inlet mass flow rate equals the outlet mass flow rate. Thus no transportation delay occurs. Vapor working fluid occurs in two locations: (i) between the evaporators and turbine, and (ii) between the turbine and condenser. Between the evaporators and the turbine, a compressible pipe model is used, which utilizes the mass flow difference between inlet and outlet to account for transportation delays. The length of pipe between the turbine and condenser is short;

therefore, its transportation delay is not significant. Additionally, pressure drop is neglected in all pipes because of the smooth inner surface and their relatively large diameter (18mm).

Given the assumption of liquid incompressibility, working fluid vapor holistically accounts for compressible effects in the high pressure section of the ORC system (everything located between the pump and the turbine). This concept was previously utilized by [9].

The compressible volume calculates the pressure, temperature and working fluid mass between the evaporators and the turbine. Mass balance and energy balance of the compressible volume is given as follows [27]:

$$\frac{dm}{dt} = \dot{m}_{in} - \dot{m}_{out}$$

(6.1)

$$u\frac{dm}{dt} + mc_v\frac{dT}{dt} = \dot{H}_{in} - \dot{H}_{out}$$

(6.2)

where m is mass, T is temperature, $\dot{m}_{in}$ and $\dot{m}_{out}$ are inlet and outlet mass flow rate, u is specific internal energy, c_v is specific heat capacity, $\dot{H}_{in}$ and $\dot{H}_{out}$ are inlet and outlet enthalpy flowrate. In order to calculate pressure, the vapor working fluid is assumed to be an ideal gas [27]:

$$\frac{RT}{V}\frac{dm}{dt} + \frac{p}{T}\frac{dT}{dt} - \frac{dp}{dt} = 0$$

(6.3)

where R is ideal gas constant, V is vapor volume. Thus, temperature, mass and pressure can be solved by combining equations (6.1), (6.2), (6.3).

Expander

In the current configuration, a turbine expander is connected to an electric generator. Relative to displacement expanders, turbine expanders mate well with electric generators [28]. For the turbine expander, working fluid mass flow rate, $\dot{m}_{expander}$, is a function of turbine speed, $N_{expander}$, and pressure ratio, $\frac{p_{in}}{p_{out}}$, from [29] as follows:

$$\dot{m}_{expender} = f(N_{expender}, \frac{p_{in}}{p_{out}})$$

(7.1)

Outlet temperature, T_{out}, can be calculated based on the thermodynamic principle [27]:

$$T_{out} = T_{in}\left[1 - \eta_{is}\left(1 - \left(\frac{p_{out}}{p_{in}}\right)^{\frac{\gamma-1}{\gamma}}\right)\right]$$

(7.2)

where η_{is} is isentropic efficiency. For simplicity, turbine power is calculated with physics:

$$P_{Turb} = \eta_{eg}\dot{m}c_p(T_{in} - T_{out})$$

(7.3)

where η_{eg} is electrical generator efficiency.

Reservoir

The reservoir serves as an ORC system transient buffer, guaranteeing enough liquid working fluid to avoid pump cavitation effects. Mass balance and energy balance are considered in the reservoir model.

$$\frac{dm}{dt} = \dot{m}_{in} - \dot{m}_{out}$$

(8.1)

$$\frac{dmh}{dt} = \dot{m}_{in}h_{in} - \dot{m}_{out}h_{out}$$

(8.2)

where h_{in} and h_{out} are inlet and outlet fluid enthalpy, and h is enthalpy in the reservoir. Meanwhile, the reservoir level is calculated from eq. (8.3):

$$Lev = \frac{m}{m_0}$$

(8.3)

where m_0 represents working fluid mass when reservoir is full of liquid working fluid.

Junctions

The ORC-WHR system includes four junctions: a split junction before two evaporators, a combination junction after two evaporators, a split junction before turbine, and a combination junction after turbine. Mass balance and energy balance are applied to those four junctions as shown below.

$$\dot{m}_{sum} = \dot{m}_1 + \dot{m}_2$$

(9.1)

$$\dot{m}_{sum}h_{sum} = \dot{m}_1h_1 + \dot{m}_2h_2$$

(9.2)

Model Identification

Empirical parameters are obtained from model identification. If the system set-up is changed, those empirical parameters need to be identified again. All physical parameters are directly measured, such as heat exchanger area, evaporator wall mass, etc. Identification of each component model is discussed individually.

Pump

A positive displacement pump is used in the system. Mass flow rate is nearly linear with respect to pump speed for the characteristic of displacement pump. Coefficients a_{pump} and b_{pump} are fitted from manufacturer pump mass flow data. as shown in Figure 2.
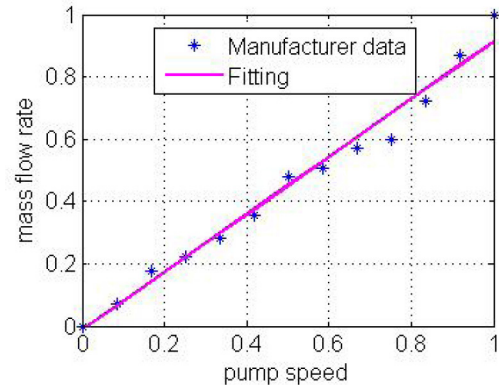

Figure 2. High pressure pump mass flow rate (normalized by maximum value)

Expander

The only parameter to be identified in the expander model is isentropic efficiency from eq. (7.2). While isentropic efficiency is a function of pressure ratio and turbine speed, a constant isentropic efficiency of 0.6 is identified for the range of conditions covered by the experimental data.

Valves with Incompressible Liquid - Mass Flow to the Evaporators

Two coefficients are identified for the two mass flow distribution valves: $c_{EvapVlv}$ and $a_{EvapVlv}$. Evaporator mass flow rates, high pressure pump speed, and valve opening data are utilized for this purpose. The identification results are: $c_{EvapVlv} = 0.5218$, and $a_{EvapVlv} = 1$.
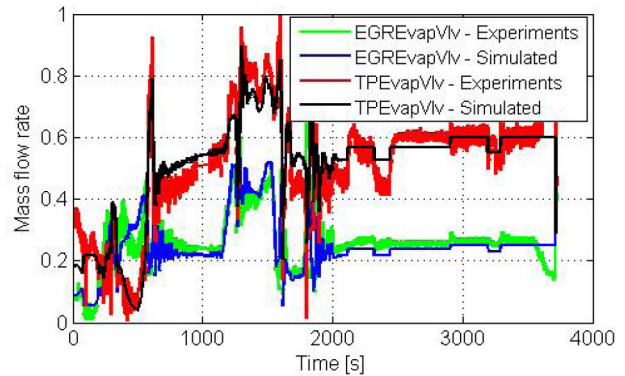

Figure 3. Mass flow rate through the TP and EGR evaporator distribution valves (normalized by maximum value)

The experimental data used to identify the mass flow distribution valve coefficients are obtained at transient engine conditions, including an engine cold start and ORC warm-up event; quasi steady engine operation at 1200RPM, 1000Nm; 1600RPM, 1000Nm; 1600RPM, 1250Nm; 1200 RPM, 1000Nm; several alterations to working fluid vapor setpoint temperature; and ORC cool down. This data set subjects the ORC system to three distinct states: warm-up, regular operation, and cool-down. Figure 3 shows the identification data set. The ORC system warm-up stage occupied the first 1200 seconds until the desired working fluid temperature and pressure setpoint was reached. Then, transient conditions were investigated from 1200 seconds to 1600 seconds. After that, engine conditions were fixed at 1200RPM and 1000Nm, while the high pressure pump was manipulated with several

step changes of command. Model identification results are also shown in <u>Figure 3</u>, indicating substantial agreement with experimental data well even during the high transient situation.

Valves with Compressible Vapor - Mass Flow to the Expander

Discharge coefficients for compressible vapor working fluid flow through the turbine upstream and turbine bypass valves need to be identified. Several measurements are required to accomplish this: pressure before and after each valve, working fluid mass flow, and the valve opening areas. Experimental data used for turbine bypass valve identification consists of 24 steady state points taken at two engine speeds and two torque levels: 1000RPM, 1039Nm; and 1200RPM, 1000Nm; with three EGR rates: 8%, 12%, 17% at each speed/load point. Furthermore, four turbine upstream working fluid vapor setpoint temperatures are commanded at each operating condition.

Discharge coefficient results from these experiments are shown in <u>Figure 4</u>. The curve fit captures the experimental data trend, although the maximum relative error is as large as 10%. The results shown in <u>Figure 4</u> have a fixed evaporating pressure at 20bar. Experimental data is limited for other operating pressures. Therefore, a multiplier $\left(p_{evap}/d_{V1}\right)$ is applied to the discharge coefficient, allowing simulation of other vapor pressures, which is shown in <u>eq. (10.1)</u>. As experimental data across a variety of working fluid vapor pressures become available, a 3D map will be created for discharge coefficient.

$$C_{d,TurbBypVlv} = \left(a_{V1}O_{TurbBypVlv}^2 + b_{V1}O_{TurbBypVlv} + c_{V1}\right)\cdot\left(\frac{p_{evap}}{d_{V1}}\right)$$

(10.1)

The turbine upstream valve is expected to be fully open during power generation; therefore its identification focuses on the fully open condition and is a linear function of pressure <u>eq. (10.2)</u>.
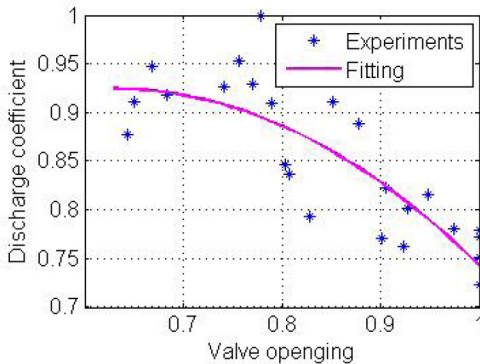
$$C_{d,TurbUpVlv} = a_{V2}p_{evap}$$

(10.2)

Figure 4. Turbine upstream valve and turbine bypass valve discharge coefficient

Evaporators and Condenser

Due to discrepancies between the physical evaporator design and the empirical heat transfer correlations available in literature, heat transfer coefficient and evaporator efficiency multipliers are utilized for model identification. The efficiency multiplier accounts for heat losses from evaporator to environment, whereas the heat transfer

coefficient multiplier accounts for the complex structure of the experimental heat exchanger relative to the geometry for which the correlations were derived.

Heat exchanger identification utilized mass flow rates into each evaporator (both working fluid and exhaust/EGR gases), in addition to temperature and pressure measurements upstream and downstream of the evaporators (again, both for the working fluid and the exhaust/EGR). The experimental data set utilized for evaporator and condenser parameter identification are the same data used in turbine bypass valve discharge coefficient identification, consisting of 24 ORC system steady state points.

Each evaporator model is identified separately by providing the experimental inlet conditions for the working fluid and the respective heat source. Simulated evaporator outlet states for the heat source flow and the working fluid are then compared with experimental results for the same inputs. The efficiency multiplier and heat transfer coefficient multiplier are identified by minimizing the error between simulation and experiments. Error is defined based on both exhaust outlet temperature error and working fluid outlet temperature error as shown in <u>eq. (11.1)</u>.

At each steady state condition, error is plotted as a function of efficiency multiplier and heat transfer coefficient multiplier as shown in <u>Figure 5</u>. The pair of parameters which produces minimum error was selected as identified value corresponding to that steady state condition. A sample identification error map, for a single steady state condition, is given in <u>Figure 5</u>.

$$e = \frac{\sqrt{\left(h_{f,out,TP,sim} - h_{f,out,TP,exp}\right)^2 + \left(h_{e,out,TP,sim} - h_{e,out,TP,exp}\right)^2}}{\sqrt{h_{f,out,TP,exp}^2 + h_{e,out,TP,exp}^2}} \times 100\%$$
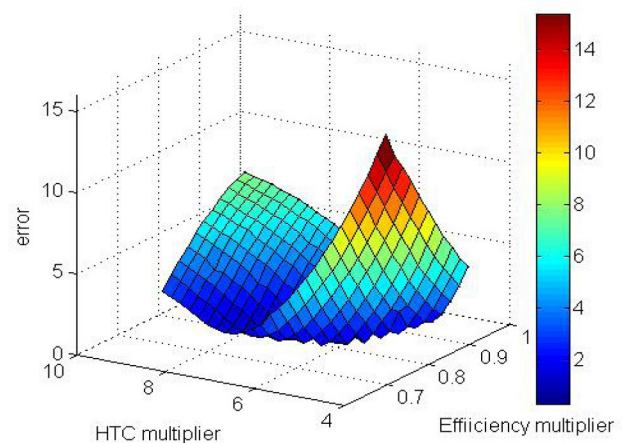
(11.1)

Figure 5. Error of evaporator efficiency multiplier and heat transfer coefficient multiplier identification

Correlations fit the identified coefficients across all steady state data points according to <u>eq. (11.2)</u>, <u>(11.3)</u>, <u>(11.4)</u>, <u>(11.5)</u>. Four parameters are considered as variables for each evaporator efficiency multiplier and heat transfer coefficient multiplier correlation: the mass flow rates and temperatures of the working fluid and heat source gases. <u>Figure 6</u> exhibits comparisons of identification results where the horizontal axis is the multiplier calculated from experimental values

and vertical axis is the multiplier from the identified correlation. In Figure 6, TP heat transfer coefficient (HTC) multiplier correlation shows strong alignment with experimental data, its predictions being within ~5% of measured values. EGR efficiency multiplier exhibits very good trend-wise agreement, although some of the identified points vary by as much as 10%.

$$m_{\eta,TP} = 53.16\dot{m}_{f,TP} + 0.004685\frac{T_{f,up,TP}+T_{f,down,TP}}{2} - 2.213$$

$$(11.2)$$

$$m_{U,TP} = -4.522\dot{m}_{e,TP} + 0.01295\frac{T_{f,up,TP}+T_{f,down,TP}}{2} + 1.146$$

$$(11.3)$$

$$m_{\eta,EGR} = 96.93\dot{m}_{f,EGR} - 0.01866\frac{T_{e,up,EGR}+T_{e,down,EGR}}{2} + 10.7$$

$$(11.4)$$

$$m_{U,EGR} = -66.19\dot{m}_{e,EGR} - 0.01402\frac{T_{f,up,EGR}+T_{f,down,EGR}}{2} + 13.62$$
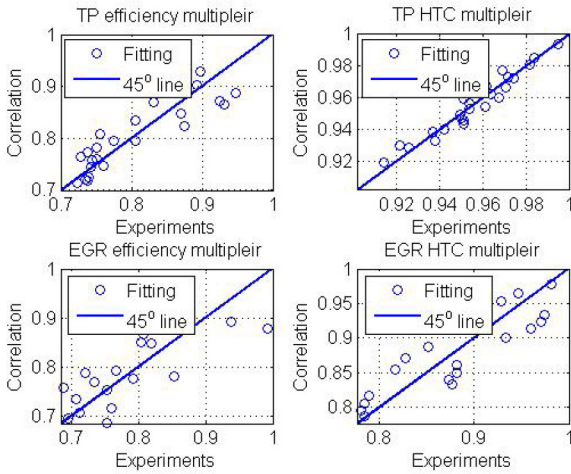
$$(11.5)$$

Figure 6. TP & EGR evaporator identification results (normalized by maximum value)

Model Validation

The ORC system model developed and calibrated in previous sections is validated over two transient operating conditions, namely a step-change of the turbine upstream temperature, and a simultaneous increase of engine load & speed.

For the validation study, the relative error is defined by eq. (12.1).

$$e_r = \frac{|sim-exp|}{|exp|} \times 100\%$$

$$(12.1)$$

Validation under Transient Operating Conditions - 1

In the first transient scenario, the turbine upstream mixed vapor temperature undergoes a step change of 20K. This is carried out at a fixed engine operating condition of 1200RPM, 1000Nm, and 17% EGR rate. The ORC model uses inputs from the experiments, which

include: tail pipe and EGR heat source mass flow rates and temperatures measured before the evaporators, high pressure pump speed, working fluid mass flow valve openings, turbine bypass valve opening, and the tail pipe bypass valve opening. The turbine upstream valve is fully closed during this transient. Condenser coolant pump speed is not included because of the assumption of infinite cooling capacity. Some of the model inputs are plotted in Figure 7.

A comparison of simulation and experimental results for transient condition 1 (mixed vapor temperature step change) are shown in Figure 8. For the ORC-WHR system model, the two most important states are mixed vapor temperature and evaporating pressure, which directly affect how much power can be generated from the expander. In Figure 8, the simulated working fluid mixed vapor temperature is able to track both the trend and magnitude of experimental result with average error of only 3.3%. Simulated mixed vapor temperature displays a small undershoot during the transient, which may indicate lower component thermal inertia in the model relative to the real evaporator.
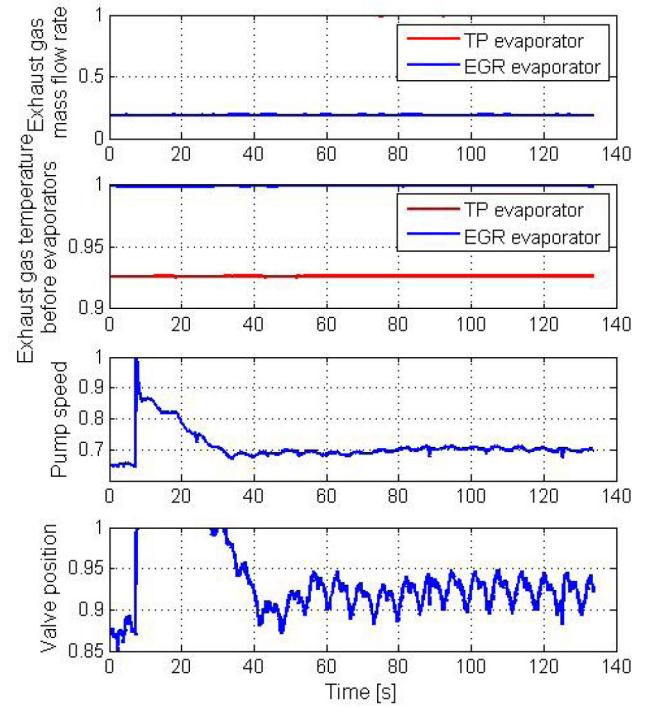

Figure 7. Inputs to the model at transient condition 1 (normalized by maximum value)

Validation under Transient Operating Conditions - 2

The engine undergoes a transient from 1200RPM, 1000Nm, 21% EGR to 1580RPM, 1250Nm, 19% EGR. During this event, the turbine upstream valve is fully open and the turbine bypass valve is fully closed. The turbine upstream vapor temperature is experimentally maintained at a desired setpoint via a PID control of the high pressure pump speed. Pertinent 'Transient 2' inputs are plotted in Figure 9.

Simulation and experimental results comparison for 'transient condition 2' are shown in Figure 10. During the 1300 second test, both the TP and EGR mass flow distribution valve models predict

mass flow well, and follow experimental values within 5.2% and 9.2% respectively. Turbine upstream mixed vapor temperature results are presented in the second plot in Figure 10. Trend tracking is not perfect, especially from 200-350 seconds and again from 700-800 seconds. However, the average error is approximately 2.3%, which is accurate enough for system optimization.
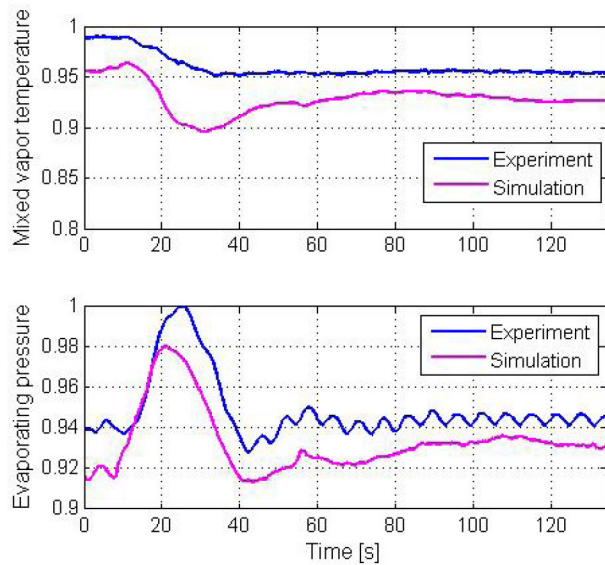
predicts the turbine generated power trend well, with an average error of only 1.7%. Note that the turbine power trend displays the same profile as evaporating pressure and pump speed (Figure 9), rather than the turbine upstream mixed vapor temperature.

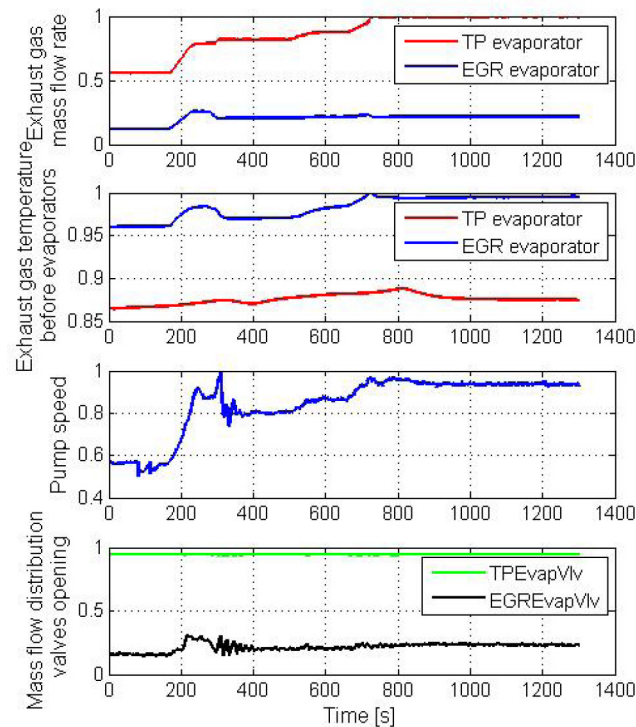Figure 8. Simulation and experimental results at transient condition 1 (normalized by maximum value)

Figure 9. Inputs to the model at transient condition 2 (normalized by maximum value)

Experimental measurements of turbine power output were not available. Therefore turbine power is calculated by applying experimental data to eq. (7.3). The bottom two plots in Figure 10 show the evaporating pressure and turbine generated power. Predicted evaporating pressure tracks the experimental trend very well but experiences a nearly constant offset error of 12%. The model also
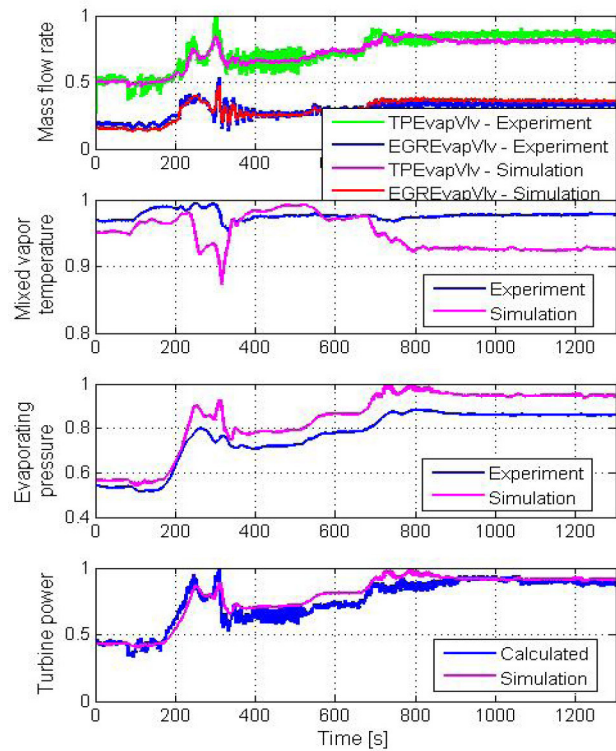

Figure 10. Simulation and experimental results at transient condition 2 (normalized by maximum value).
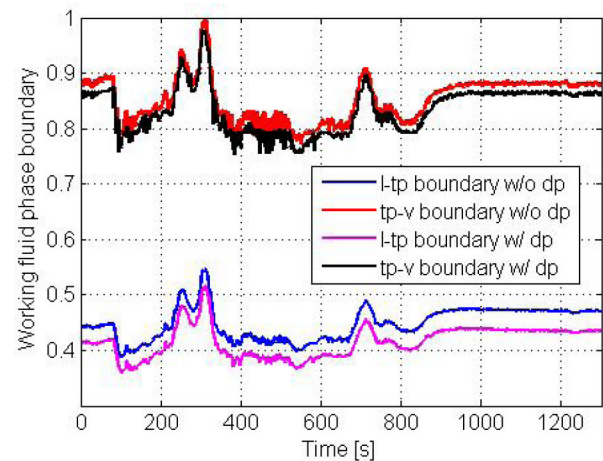

Figure 11. Comparison of working fluid phase boundary locations (expressed as normalized length) within the TP evaporator between the baseline model (w/o dp) and new model (w/ dp) at transient condition 2.

To illustrate the impact of including the pressure drop in the evaporator model, the working fluid phase boundary locations within the TP evaporator are plotted in Figure 11, with and without pressure drop (dp). With the pressure drop model, liquid-two phase and two phase-vapor boundaries advance along the evaporator length by 7.1% and 2.1% respectively. Since the degree of working fluid superheating is proportional with the length of the vapor phase within each evaporator, the inclusion of evaporator pressure drop is important for accurate vapor quality prediction, which hence transient control and ORC power maximization.

Discussion

The model validation results are reasonable and instill confidence for the utilization of the physics-based model moving forward. The only variable displaying a higher than expected estimation error is vapor temperature, and it may be due to a combination of several of the following factors.

The turbine upstream vapor temperature is sensitive to total working fluid mass flow rate, with lower working fluid mass flow rates producing higher mixed vapor temperatures and vice versa. Therefore, the high pressure pump model parameters play an important role in the mixed vapor temperature estimation.

In addition, mixed vapor temperature upstream of the turbine is sensitive to the respective distribution of working fluid mass flow rate through the TP and EGR evaporators. Errors in the distribution of working fluid mass flow influence the final mixed vapor temperature due to the disparity in heat source power levels. In Figure 3, the estimated working fluid mass flows deviate from experimental results between 300-500 seconds and 1300-2000 seconds. In order to reduce mixed vapor temperature prediction error, improvements to the mass flow rate distribution valve correlations are needed.

Evaporator efficiency identification also plays an important role in the mixed vapor temperature estimation. A one percent TP evaporator efficiency change results in a 4K change of TP outlet vapor temperature, which will have an impact on the mixed vapor temperature and produced power proportional to the TP evaporator working fluid mass flow relative to total mass flow.

Experimental evaporating pressure trends are captured well by the model over the two transient validation conditions. In transient condition 1, the average error is 1.7%, indicating that the turbine bypass valve discharge coefficients are highly accurate. In the transient condition 2, the average evaporating pressure error is as large as 12.7%, which results from the identification of the turbine upstream valve discharge coefficient at 100% opening. This error is almost constant along the transient 2 condition, but it should be straightforward to overcome with better identification of the turbine upstream valve.

The model presents good performance in the prediction of turbine generated power with the average error 1.7% over the transient condition 2. Generated power predictions depend on all ORC system submodels; therefore, the accurate prediction of power exhibited by this physics-based ORC system model bodes well for real-world applicability in both offline and online.

Thermal inertia of the evaporator plays a vital role in vapor temperature dynamic response. The current model approximates the wall as a single layer between the working fluid and exhaust gas. More layers can be considered to enhance wall heat transfer performance [30].

Conclusions

A high-fidelity ORC-WHR system model developed in this study includes a low pressure working fluid supply pump, a high pressure pump, evaporators in the TP and EGR streams, valves which distribute the working fluid between the Tailpipe and EGR branches, an exhaust bypass valve, a valve upstream of the turbine expander, turbine bypass valve, turbine expander, a condenser downstream of the turbine, and an expansion tank. A finite volume method is used to model the evaporator, and a pressure drop model is included to improve accuracy of predictions.

Model parameter identification is carried out using experimental measurements on an ORC system coupled to a 13L heavy duty diesel engine. Evaporator efficiency multiplier and heat transfer coefficient multiplier are introduced to capture discrepancies between the physical evaporator design and idealized designs used for developing empirical correlations available in literature.

Model fidelity was validated under transient operating conditions. The first transient event included a step-change of turbine upstream mixed vapor temperature, and the second transient event was induced by a step-change of engine speed & load. Validation results show the model's ability to accurately predict: working fluid mass flow rate, vapor temperature in both TP and EGR evaporators, vapor temperature before the turbine expander and working fluid evaporating pressure. The average error over a transient event for all aforementioned variables was within 10% and in most cases was below 5%. Several suggestions are made to improve the model accuracy: identification of evaporator efficiency over a wider range of conditions experienced during transients, turbine upstream valve identification over a wider range of vapor pressures, consideration of reservoir heat loss, and inclusion of a detailed evaporator wall model.

The inclusion of an evaporator pressure drop model improves the prediction of working fluid phase boundaries, thus allowing: (i) increased accuracy of the working fluid vapor temperature at the evaporator exit, (ii) greater resolution of vapor quantity within the evaporator for transient control, and (iii) enhanced prediction of vapor superheating for transient control and power maximization.

The high-fidelity model presented in this paper will be utilized for future offline optimization and co-simulations. Additionally, it can serve as basis for model reduction, and development of control-oriented ORC models, optimization of ORC power generation and model-based control.

References

1. EPA, "EPA and NHTSA adopt first-ever program to reduce greenhouse gas emissions and improve fuel efficiency of medium- and heavy-duty vehicles," 2011.

2. ICCT, "UNITED STATES EFFICIENCY AND GREENHOUSE GAS EMISSION REGULATIONS FOR MODEL YEAR 2018-2027 HEAVY-DUTY VEHICLES, ENGINES, AND TRAILERS," 2015.

3. Arias, D., Shedd, T., and Jester, R., "Theoretical Analysis of Waste Heat Recovery from an Internal Combustion Engine in a Hybrid Vehicle," SAE Technical Paper 2006-01-1605, 2006, doi:10.4271/2006-01-1605.

4. Endo, T., Kawajiri, S., Kojima, Y., Takahashi, K. et al., "Study on Maximizing Exergy in Automotive Engines," SAE Technical Paper 2007-01-0257, 2007, doi:10.4271/2007-01-0257.

5. Teng, H., Regner, G., and Cowland, C., "Achieving High Engine Efficiency for Heavy-Duty Diesel Engines by Waste Heat Recovery Using Supercritical Organic-Fluid Rankine Cycle," SAE Technical Paper 2006-01-3522, 2006, doi:10.4271/2006-01-3522.

6. Park, T., Teng, H., Hunter, G., van der Velde, B. et al., "A Rankine Cycle System for Recovering Waste Heat from HD Diesel Engines - Experimental Results," SAE Technical Paper 2011-01-1337, 2011, doi:10.4271/2011-01-1337.

7. Dieter, S., Thomas, L., Jurgen, G., Nadja, E., et al, "Waste heat Recovery for Commercial Vehicles with a Rankine Process," 21st Aachen Colloquium Automobile and Engine technology, 2012.

8. Quoilin, S., "Sustainable Energy Conversion Through the Use of Organic Rankine Cycles for Waste Heat Recovery and Solar Applications," PhD Thsis, University of Liege, 2011.

9. Feru, E., de Jager, B., Willems, F., and Steinbuch, M., "Modeling and Control of a Parallel Waste Heat Recovery System for Euro-VI Heavy-Duty Diesel Engines," *Energies*, vol. 7, pp. 6571-6592, 2014/10/14/ 2014.

10. Manglik, R., and Bergles, A., "Heat-Transfer and Pressure-Drop Correlations for the Rectangular Offset Strip Fin Compact Heat-Exchanger," *Experimental Thermal and Fluid Science*, vol. 10, pp. 171-180, Feb 1995.

11. Wang, X., and Mujumdar, A., "Heat transfer characteristics of nanofluids: a review," *International Journal of Thermal Sciences*, vol. 46, pp. 1-19, Jan 2007.

12. Yamamoto, T., Furuhata, T., Arai, N., and Mori, K., "Design and testing of the Organic Rankine Cycle," *Energy*, vol. 26, pp. 239-251, Mar 2001.

13. Tona, P., Peralez, J., and Sciarretta, A., "Supervision and control prototyping for an engine exhaust gas heat recovery system based on a steam Rankine cycle," 2012 Ieee/Asme International Conference on Advanced Intelligent Mechatronics (Aim), pp. 695-701, 2012.

14. Feru, E., Willems, F., de Jager, B., and Steinbuch, M., "Model predictive control of a waste heat recovery system for automotive diesel engines," in System Theory, Control and Computing (ICSTCC), 2014 18th International Conference, 2014, pp. 658-663.

15. Hou, G., Bi, S., Lin, M., Zhang, J., and Xu, J., "Minimum variance control of organic Rankine cycle based waste heat recovery," *Energy Conversion and Management*, vol. 86, pp. 576-586, Oct 2014.

16. Peralez, J., Tona, P., Sciarretta, A., Dufour, P., et al, "Towards model-based control of a steam Rankine process for engine waste heat recovery," 2012 Ieee Vehicle Power and Propulsion Conference (Vppc), pp. 289-294, 2012.

17. Qiao, H., Aute, V., and Radermacher, R., "An Improved Moving Boundary Heat Exchanger Model with Pressure Drop," International Refrigeration and Air Conditioning Conference, 2014/01/01/ 2014.

18. Wang, R., Zhao, X., Wang, C., and Li, Y., "Modeling and model order reduction of evaporator in organic rankine cycle for waste heat recovery," in *2011 International Conference on Advanced Mechatronic Systems (ICAMechS)*, 2011, pp. 291-296.

19. Horst, T., Rottengruber, Seifert, H., and Ringler, J., "Dynamic heat exchanger model for performance prediction and control system design of automotive waste heat recovery systems," *Applied Energy*, vol. 105, pp. 293-303, 2013/05// 2013.

20. Carey, V., Liquid Vapor Phase Change Phenomena: An Introduction to the Thermophysics of Vaporization and Condensation Processes in Heat Transfer Equipment, Second Edition, 2 edition ed. New York: CRC Press, 2007.

21. Reynolds, O., "An Experimental Investigation of the Circumstances Which Determine Whether the Motion of Water Shall Be Direct or Sinuous, and of the Law of Resistance in Parallel Channels," *Philosophical Transactions of the Royal Society of London*, vol. 174, pp. 935-982, 1883/01/01/ 1883.

22. Gnielinski, V., "Berechnung des Druckverlustes in glatten konzentrischen Ringspalten bei ausgebildeter laminarer und turbulenter isothermer Strömung," *Chemie Ingenieur Technik*, vol. 79, pp. 91-95, 2007/02/01/ 2007.

23. Blaß, E., and Chemieingenieurwesen G. V. u., VDI-Gesellschaft Verfahrenstechnik und Chemieingenieurwesen GVC: gestern, heute, morgen; eine Jubiläumsschrift anläßlich des Jahrestreffens der Verfahrensingenieure 1984 in München zum 50-jährigen Bestehen der GVC: Saur, 1984.

24. Bergman, T., Incropera, F., and Lavine, A., *Fundamentals of Heat and Mass Transfer*: John Wiley & Sons, 2011.

25. Zivi, S., "Estimation of Steady-State Steam Void-Fraction by Means of the Principle of Minimum Entropy Production," *Journal of Heat Transfer*, vol. 86, pp. 247-251, 1964/05/01/ 1964.

26. Weiss, H., and Boshwirth, L., "A Simple but Efficient Equipment for Experimental Determination of valve Loss Coefficient Under Compressible and Steady Flow Condtions," in International Compressor Engineering Conference, 1982, pp. 69-76.

27. Michael, J., and Howard, S., *Fundamentals of Engineering Thermodynamics*, 5th ed.: John Wiley & Sons, Inc, 2006.

28. Teng, H., Klaver, J., Park, T., Hunter, G. et al., "A Rankine Cycle System for Recovering Waste Heat from HD Diesel Engines - WHR System Development," SAE Technical Paper 2011-01-0311, 2011, doi:10.4271/2011-01-0311.

29. Moraal, P. and Kolmanovsky, I., "Turbocharger Modeling for Automotive Control Applications," SAE Technical Paper 1999-01-0908, 1999, doi:10.4271/1999-01-0908.

30. Feru, E., de Jager, B., Willems, F., and Steinbuch, M., "Two-phase plate-fin heat exchanger modeling for waste heat recovery systems in diesel engines," *Applied Energy*, vol. 133, pp. 183-196, Nov 15 2014.

31. Blasius, H., "Das Aehnlichkeitsgesetz bei Reibungsvorgängen in Flüssigkeiten," in *Mitteilungen über Forschungsarbeiten auf dem Gebiete des Ingenieurwesens*. vol. 131, ed: Springer Berlin Heidelberg, 1913, pp. 1-41.

32. Lockhart, R., and Martinelli, R., "Proposed correlation of data for isothermal two-phase, two-component flow in pipes," *Chem. Eng. Prog*, vol. 45, pp. 39-48, 1949 1949.

Appendix

Appendix

Pressure drop is derived based on the fundamentals of momentum balance. For a two-phase situation, an idealized model of momentum transport is shown below,
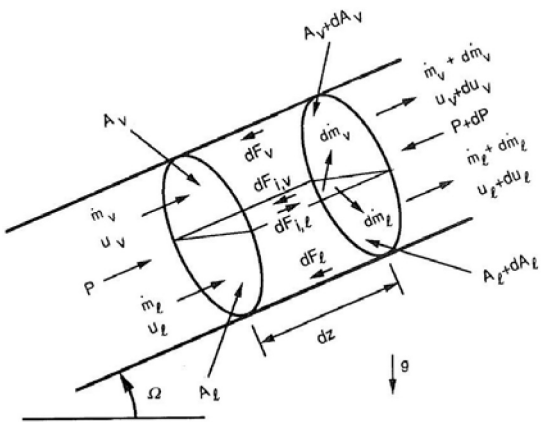

Figure 12. Idealized model of momentum transport during two-phase flow in an inclined tube[20]

In Figure 12, v and l are vapor and liquid respectively, Ω is the angle between flow speed direction and horizontal line, g is the gravitational acceleration, u is flow velocity, z is axial location, and F is wall frictional force. In dz unit, apply force balance to vapor and liquid respectively

$$pA_v - (p + dp)(A_v + dA_v) - dF_v - dF_{i,v} - A_v dz \rho_v g \sin\Omega - d\dot{m}_l u_l = (\dot{m}_v + d\dot{m}_v)(u_v + du_v) - \dot{m}_v u_v$$

(2.5)

$$pA_l - (p + dp)(A_l + dA_l) - dF_l - dF_{i,l} - A_l dz \rho_l g \sin\Omega + d\dot{m}_l u_l = (\dot{m}_l + d\dot{m}_l)(u_l + du_l) - \dot{m}_l u_l$$

(2.6)

According to Newton's third law:

$$dF_{i,v} = -dF_{i,l}$$

(2.7)

Total section area can be expressed by the sum of vapor section area and liquid section area:

$$A = A_v + A_l$$

(2.8)

Combine eqs. (2.5), (2.6), (2.7), (2.8):

$$-Adp - pdA - dF_l - dF_v - (A_l \rho_l - A_v \rho_v)gdz \sin\Omega = d(\dot{m}_v u_v + \dot{m}_l u_l)$$

(2.9)

Define friction force [20]:

$$-\left(\frac{dp}{dz}\right)_{fr} Adz = dF_l + dF_v$$

(2.10)

Speed of vapor and liquid can be expressed as [20]:

$$u_v = \frac{Gx}{\rho_{vap}\alpha}$$

(2.11)

$$u_l = \frac{G(1-x)}{\rho_{sat}(1-\alpha)}$$

(2.12)

Where x is vapor quality, G is mass flux. Void fraction is defined as:

$$\alpha = \frac{A_v}{A}$$

(2.13)

Combining eq. (2.9), (2.10), (2.11), (2.12), (2.13), two-phase pressure drop can be derived:

$$-\left(\frac{dp}{dz}\right)_{tp} = -\frac{p}{A}\left(\frac{dA}{dz}\right) - \left(\frac{dp}{dz}\right)_{fr} + \left[(1-\alpha)\rho_{sat} + \alpha\rho_{vap}\right]g \cdot \sin\Omega + \frac{1}{A}\frac{d}{dz}\left[\frac{G^2 x^2 A}{\rho_{vap}\alpha} + \frac{G^2(1-x)^2 A}{\rho_{sat}(1-\alpha)}\right]$$

(2.14)

eq. (2.14) can be rewritten as follows:

$$0 = \left[\left(\frac{dp}{dz}\right)_{tp} - \frac{p}{A}\left(\frac{dA}{dz}\right)\right] + \left[-\left(\frac{dp}{dz}\right)_{fr}\right] + \left[\left[(1-\alpha)\rho_{sat} + \alpha\rho_{vap}\right]g \cdot \sin\Omega\right] + \frac{1}{A}\frac{d}{dz}\left[\frac{G^2 x^2 A}{\rho_{vap}\alpha} + \frac{G^2(1-x)^2 A}{\rho_{sat}(1-\alpha)}\right]$$

(2.15)

eq. (2.15) is the detail form of eq. (1.5). For pure liquid region and pure vapor region, vapor quality equals to 0 and 1 respectively.

$$x_l = 0, x_v = 1$$

(2.16)

Substitute eq. (2.16) into eq. (2.15). Pure liquid pressure drop and pure vapor pressure utilize the same equational form, which is named single phase region pressure drop:

$$-\left(\frac{dp}{dz}\right)_s = -\frac{p}{A}\left(\frac{dA}{dz}\right) - \left(\frac{dp}{dz}\right)_{fr,s} + \rho g \sin\Omega + \frac{1}{A}\frac{d}{dz}\left(\frac{G^2 A}{\rho}\right)_s$$

(2.17)

where $\frac{dp}{dx}$ is pressure gradient, and $\frac{dA}{dx}$ is sectional area gradient, which equals to zero for the evaporators in the experiments. For single-phase flow in round tubes, the frictional pressure gradient can be evaluated in terms of friction factor [20]:

$$-\left(\frac{dp}{dz}\right)_{fr,s} = \frac{2f_s G_s^2}{\rho_s d_h}$$

(2.18)

where f_s is friction factor, which can be determined from well-known Blasius correlation [31]:

$$f_s = B\,Re^{-n} = B\left(\frac{G_s d_h}{\mu_s}\right)^{-n}$$

(2.19)

where subscript s means single-phase, B and n depends on flow pattern. B=16, n=1 for laminar flow, and B=0.079, n=0.25 for turbulent flow. For two-phase frictional pressure, it can be derived from single-phase with a multiplier and vapor phase is chosen in this paper with no reason.

$$-\left(\frac{dp}{dz}\right)_{fr,tp} = \varphi_v\left[-\left(\frac{dp}{dz}\right)_{fr,v}\right] = \varphi_v\frac{2f_v G_v^2}{\rho_v d_h}$$

(2.20)

Where φ_v is the two-phase multiplier, which is defined by Lockhart and Martinelli [32]:

$$\varphi_v = 1 + CX + X^2$$

(2.21)

$$X = \left[\frac{\left(\frac{dp}{dz} \right)_l}{\left(\frac{dp}{dz} \right)_v} \right]^{0.5}$$

(2.22)

Table 1. Constant C value at different flow pattern

Liquid	Gas	C
Turbulent	Turbulent	20
Laminar	Turbulent	12
Turbulent	Laminar	10
Laminar	Laminar	5

Where X is the Martinelli parameter and C is constant depending on flow pattern. Apply eq. (2.18) and (2.19) to both liquid and vapor:

$$\left(\frac{dp}{dz} \right)_l = \frac{2 f_l G^2 (1-x)^2}{\rho_l d_h}$$

(2.23)

$$f_l = B \, Re_l^{-n} = B \left(\frac{G(1-x) d_h}{\mu_l} \right)^{-n}$$

(2.24)

$$\left(\frac{dp}{dz} \right)_v = \frac{2 f_v G^2 x^2}{\rho_v d_h}$$

(2.25)

$$f_v = B \, Re_v^{-n} = B \left(\frac{G x d_h}{\mu_v} \right)^{-n}$$

(2.26)

Substitute above four equations into X. X can be expressed:

$$X = \left[G^{(n_v - n_l)} d_h^{(n_v - n_l)} \frac{B_l}{B_v} \frac{(1-x)^{(2-n_l)}}{(x)^{(2-n_v)}} \frac{\mu_v^{(-n_v)}}{\mu_l^{(-n_l)}} \frac{\rho_v}{\rho_l} \right]^{0.5}$$

(2.27)

Regarding the gravity term in the pressure drop expression: (i) When the working fluid flows upwards, gravitational force is drag force for the flow. (ii) When the working fluid flows downwards, gravitational force is positive force for the flow. Therefore, the gravitational force effect on the pressure drop can be cancelled both in single-phase and two-phase for a horizontally configured helical coil tube. Then, pressure drop in the liquid phase, vapor phase and two-phase can be derived:

Liquid phase region:

$$\Delta p_l = \int_{z_1}^{z_{a_{sat}}} \left(\frac{dp}{dz} \right) dz = \int_{z_1}^{z_{a_{sat}}} - \left(\frac{2 f_l G^2}{\rho_l d_h} + \frac{1}{A} \frac{d}{dz} \left(\frac{G^2 A}{\rho_l} \right) \right) dz = - \left(\sum_{i=1}^{a_{sat}} \left(\frac{2 \bar{f}_{li} \bar{G}_i^2}{\bar{\rho}_{li} d_h} \Delta z \right) + \left[\frac{G_{a_{sat}+1}^2}{\rho_{l a_{sat}+1}} \right] - \left[\frac{G_1^2}{\rho_{l1}} \right] \right)$$

(2.28)

where a is the ath boundary of the discretized evaporator and ranges from 1 to $N+1$. N is the total discretized cell number. Calculated pressure drop locates at the boundary of each cell, therefore a has $N+1$ values.

Vapor phase region:

$$\Delta p_v = \int_{z_{a_{vap}}}^{z_{N+1}} \left(\frac{dp}{dz} \right) dz = \int_{z_{a_{vap}}}^{z_{N+1}} - \left(\frac{2 f_v G^2}{\rho_v d_h} + \frac{1}{A} \frac{d}{dz} \left(\frac{G^2 A}{\rho_v} \right) \right) dz = - \left(\sum_{i=a_{vap}}^{N+1} \left(\frac{2 \bar{f}_{v,i} \bar{G}_i^2}{\bar{\rho}_{v,i} d_h} \Delta z \right) + \left[\frac{G_{N+1}^2}{\rho_{v,N+1}} \right] - \left[\frac{G_{a_{vap}}^2}{\rho_{v,a_{vap}}} \right] \right)$$

(2.29)

Two-phase region:

$$\Delta p_{tp} = \int_{z_{a_{sat}+1}}^{z_{a_{vap}-1}} \left(\frac{dp}{dz}\right) dz = -\left(\sum_{i=a_v}^{N}\left(\overline{\Phi}_v^2 \frac{2\bar{f}_v \bar{G}_i^2 \bar{x}^2}{\bar{\rho}_v d_h}\Delta z\right) + \left[\frac{G_{a_{vap}}^2 x_{a_{vap}}^2}{\rho_{v(a_{dew})}\alpha_{a_{dew}}}\right] - \left[\frac{G_{a_{sat}+1}^2 x_{a_{sat}+1}^2}{\rho_{v(a_{sat}+1)}\alpha_{a_{sat}+1}}\right] + \left[\frac{G_{a_{vap}}^2\left(1-x_{a_{vap}}\right)^2}{\rho_{l(a_{vap})}\left(1-\alpha_{a_{vap}}\right)}\right] - \left[\frac{G_{a_{sat}+1}^2\left(1-x_{a_{sat}+1}\right)^2}{\rho_{l(a_{sat}+1)}\left(1-\alpha_{a_{sat}+1}\right)}\right]\right)$$

(2.30)

The evaporator outlet pressure boundary condition together with above three pressure drop equations provide capability to calculate inlet pressure, and pressure values at the two phase boundaries within the evaporator. The average evaporating pressure in each phase can then be obtained:

$$\bar{p}_l = 0.5\Delta p_l + \Delta p_{tp} + \Delta p_v + p_{out}$$

(2.31)

$$\bar{p}_{tp} = 0.5\Delta p_{tp} + \Delta p_v + p_{out}$$

(2.32)

$$\bar{p}_v = 0.5\Delta p_v + p_{out}$$

(2.33)

$\bar{p}_l, \bar{p}_{tp}$ and $\bar{p}_v$ are pressure in each phase, which is more accurate than p_{out} as evaporating pressure. Finally, total pressure drop across the evaporator is obtained, which will be used for pressure drop model validation because pressure drop in each phase is difficult to measure while inlet and outlet pressure can be easily accessed:

$$\Delta p_{evap} = \Delta p_l + \Delta p_v + \Delta p_{tp}$$

(2.34)